13th International Symposium on Particle Image Velocimetry – ISPIV 2019
Munich, Germany, July 22-24, 2019

Simultaneous stereo PIV and MPS^3 wall-shear stress measurements in turbulent channel flow

Esther Mäteling[1*], Philipp Mattern[2], Frank Michaux[2], Wolfgang Schröder[1], Michael Klaas[1]

[1] RWTH Aachen University, Chair of Fluid Mechanics and Institute of Aerodynamics, 52062 Aachen, Germany

[2] ILA_5150 GmbH, 52066 Aachen, Germany

[*] e.maeteling@aia.rwth-aachen.de

Abstract

The simultaneous application of the micro-pillar shear-stress sensor (MPS^3) and stereo particle-image velocimetry (PIV) measurements in wall-bounded flows allows for the simultaneous time-resolved acquisition of the two-dimensional wall-shear stress (WSS) distribution and the velocity field in the outer flow. Hence, this novel approach can be used to study the footprint of the outer, large-scale motions (LSM) onto the near-wall small-scale structures. In this study, the measurements are performed in a fully developed, turbulent channel flow at a friction Reynolds number of $Re_\tau = 925$. It is shown that the accuracy of the MPS^3 is not influenced by the seeding particles that are necessary to conduct PIV measurements providing that rarely occurring, non-physical high micro pillar deflections are eliminated in the post-processing. A separation between large and small scales of the velocity fluctuations and the WSS fluctuations is performed by two-dimensional empirical mode decomposition (EMD). Subsequently, a cross-correlation analysis between the large-scale velocity fluctuations and the large-scale WSS fluctuations shows a mean inclination angle of 14.70° between the LSM in the outer layer and the large-scale footprint imposed onto the near-wall dynamics.

1 Introduction

The simultaneous spatial and temporal resolution of the two-dimensional WSS distribution and the outer flow field in experimental measurements is rather challenging. However, to broaden the knowledge of, e.g., the internal structure of turbulent wall-bounded flows, such concurrent measurements are necessary. Previous approaches, e.g, by Mathis et al. (2009) and Baars et al. (2015), used intrusive hot-wire anemometry (HWA) methods to resolve the flow field in the near-wall region and in the outer layer of a turbulent boundary layer. However, HWA possesses the disadvantages of only providing pointwise information. Moreover, this approach includes to apply Taylor's hypothesis to transform the temporal data into spatial information. An alternative, non-intrusive measurement technique to investigate the near-wall flow field is the micro-particle tracking velocimetry (μ-PTV). In principle, the combination of μ-PTV with PTV or PIV conducted in the outer flow field is an appropriate approach. Nevertheless, although μ-PTV provides highly resolved spatial data, it is not able to capture the spanwise evolution of the near-wall dynamics.
To investigate the structural organization in wall-bounded flows, recent research is focused on the different types of near-wall small-scale modulation by LSM of the outer layer using direct numerical simulations (DNS), e.g., Agostini and Leschziner (2014, 2016), and HWA measurements, e.g., Marusic and Heuer (2007) and Mathis et al. (2009). Basically, the small scales are influenced by superposition, amplitude and frequency modulation, and distortions by sweeps and ejections (Agostini and Leschziner (2014)). The superposition, i.e., the footprint of outer LSM, is experienced as a translational shift by the near-wall small scales. For a detailed analysis, a scale separation has to be performed and afterwards, a cross-correlation between the near-wall and the outer region reveals their relation and degree of interaction.
In the current study, a two-dimensional EMD is used for scale separation following Agostini and Leschziner

(2014). This algorithm, which was originally proposed by Huang et al. (1998), splits amplitude- or frequency-modulated signals into a set of Intrinsic Mode Functions (IMF) based on the local characteristic time or space scales. By comparing the EMD to other separation algorithms and taking into consideration several studies concerning its efficacy and validity, Agostini and Leschziner (2014) showed that the EMD is well suited to separate the large from the small scales. Since the energy content of the large scales is comparable to the small-scale energy at high Reynolds numbers, proper orthogonal decomposition will not lead to convincing results. Moreover, no pre-determined functional elements are needed for the EMD like for Fourier or wavelet functions.
To overcome the drawbacks of the near-wall measurement techniques mentioned above, namely HWA and μ-PTV, and to simultaneously measure the two-dimensional WSS distribution and the outer flow field with a high spatial and temporal resolution, a novel approach is introduced. The MPS^3, which measures the time-resolved, two-dimensional WSS distribution, is firstly combined with time-resolved, stereo PIV measurements that capture the outer velocity field. A detailed analysis is conducted concerning any possible influence of the seeding particles needed to perform PIV measurements on the accuracy of the MPS^3.
The novel approach enables the investigation of the near-wall small-scale modulation by outer, large-scale events under temporally and spatially resolved conditions, which to the authors' knowledge has not been performed experimentally for TCF so far and thus, offers new opportunities in this field of study. As a first step, the current investigation focuses on the most fundamental influence, the footprinting of LSM. Since the results are compared to the conclusions drawn from DNS and HWA measurements, the evaluation methods are based on the tools used in the literature. Hence, a two-dimensional EMD is used to separate the large-scale components of the WSS fluctuations and the streamwise velocity fluctuations. For each time step, a cross-correlation between the large-scale distributions reveals the spatial delay of the LSM imposed onto the near-wall dynamics and thus, the corresponding inclination angle.
This manuscript is organized as follows. First, the experimental setup will be described in detail. Subsequently, the methods to evaluate the data obtained by MPS^3 and PIV measurements will be presented. The results cover the investigation of possible influences of the seeding particles that are necessary to conduct PIV measurements on the MPS^3 as well as the analysis of the large-scale footprints imposed onto the near-wall dynamics. Finally, the results are briefly summarized and an outlook for future work is given.

2 Experimental Setup

All experiments of this study are conducted at a friction Reynolds number $Re_\tau = \frac{u_\tau h}{\nu} = 925$ in an Eiffel-type wind tunnel at the Institute of Aerodynamics that provides a fully developed, turbulent channel flow. The $2,700$ *mm* long measurement section possesses an aspect ratio of $AR = 20$ at a channel width of $w = 2,000$ *mm* and a height of $2h = 100$ *mm*. Previous PIV and laser Doppler velocimetry (LDV) measurements showed that the flow inside the measurement section is two-dimensional and fully turbulent. Tomographic PIV measurements have successfully been applied to investigate turbulent flow structures like dissipation elements (Schäfer et al. (2011)).

The experimental setup in Figure 1 combines the components that are required to conduct simultaneous, time-resolved stereo PIV measurements and two-dimensional time-resolved WSS measurements using the MPS^3. The latter consists of flexible, cylindrical structures, so-called micro pillars, made from the polymer *polydimethylsiloxane*. An exemplary image is shown in figure 1(c) with a zoom of the sensor. The MPS^3 is flush-mounted on the measurement surface and the geometry of the micro pillars is adapted to the height of the viscous sublayer ensuring only a local disturbance of the flow field. The micro pillars bend due to the exerted fluid forces and for small deflections, they can be described by linear bending theory. To obtain the WSS distribution, each MPS^3 image is compared to a reference image at zero velocity. The resulting micro pillar tip deflection is converted to the WSS based on a previously performed calibration. For a detailed description of the working principle of the MPS^3 and the calibration process, please refer to, e.g., Große et al. (2006), Große and Schröder (2009), and Liu et al. (2019).
The PIV images are acquired at a frame rate of $2,000$ Hz and the MPS^3 measurements are simultaneously performed at a frame rate of $1,000$ Hz. The different acquisition frequencies result from the fact that each MPS^3 image is recorded in between the two corresponding PIV images.
The PIV setup consists of two *Photron FASTCAM SA3* high-speed cameras placed in a stereoscopic sideward scattered arrangement. Each camera possesses a resolution of 1024×1024 px^2 and is equipped with a 180 *mm* F/3.5 *Tamron* tele macro lens. The cameras are synchronized to a *Quantronix Darwin-Duo 40*

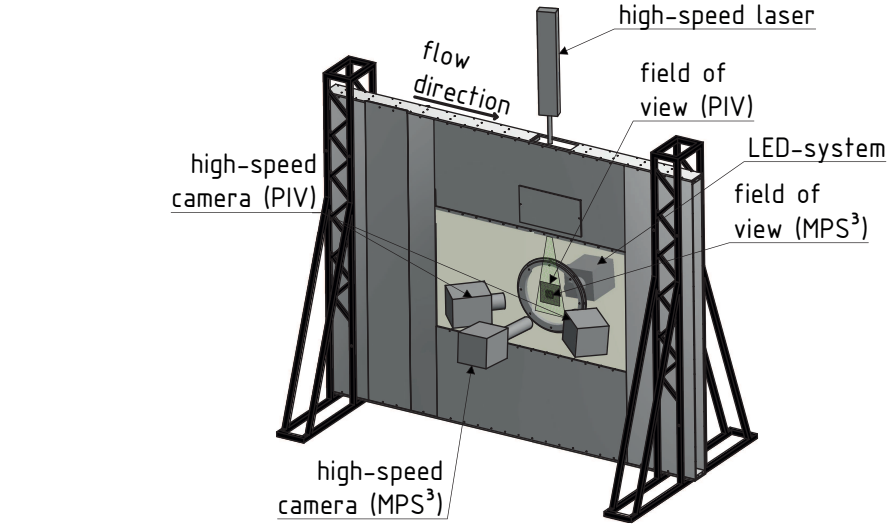

(a) isometric front view

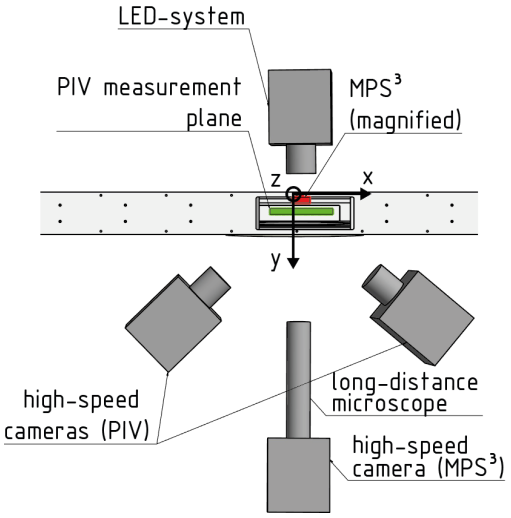

(b) measurement region along centerline, top view

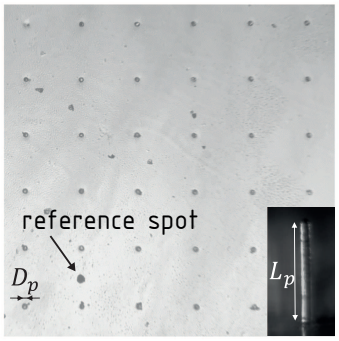

(c) extract of MPS^3, top view; sensor zoom, side view

Figure 1: Experimental setup combining MPS^3 and stereo PIV measurements.

high-speed laser. The PIV measurement plane is oriented in the streamwise direction and parallel to the channel's sidewall at a distance of $z_{PIV} = 6.25\ mm$, which corresponds to the most energetic position of the LSM $y^+ = 3.9\sqrt{Re_\tau}$ (Agostini and Leschziner (2014)). A field of view of $71 \times 56\ mm^2$ is captured by the PIV system with a resolution of approximately 13.05 px/mm in the streamwise and 15.14 px/mm in the spanwise direction. For the two-dimensional WSS measurements, an MPS^3 consisting of 9×9 micro pillars with a height of $L_p = 200\ \mu m$ and a diameter of $D_p = 14\ \mu m$ is mounted onto one channel sidewall. The micro pillars are arranged in a square with a spacing between individual micro pillars of $\Delta L_{xy} = 200\ \mu m$, which corresponds to a spatial resolution of $\Delta L_{xy}^+ \approx 3.82$. A pulsed high-power LED system in a backlight configuration is used to illuminate the MPS^3. The deflection of the micro pillars is observed in a top view through a *K2/SC long-distance microscope* lens mounted onto a *Photron FASTCAM Mini WX100* high-speed camera with a resolution of 4 Mpx. This setup yields an optical resolution of 0.96 $px/\mu m$. Wavelength separation allows the simultaneous acquisition of both flow quantities, i.e., the WSS distribution and the velocity field, and hence, the cameras are equipped with appropriate bandpass filters. Also, both measurement systems are synchronized to ensure that the instantaneous images of both systems show the same instant of time.

3 Evaluation Techniques

Since a novel approach is introduced by simultaneously measuring with PIV and the MPS^3, a thorough analysis concerning possible influences emanating from the wall-parallel velocity measurements, e.g., the seeding particles, has to be conducted. Therefore, theoretical considerations as well as comparative MPS^3 measurements with and without seeding particles are performed.
The PIV image evaluation relies on an iterative correlation scheme with subpixel accurate image deformation including background image subtraction. Since the background is slightly varying in time, a moving average based on mean and median intensity maps is subtracted from each image prior to the cross-correlation. The interrogation windows feature a size of 32×32 px^2 and an overlap of 75 % resulting in a final vector resolution of 0.5 mm.
A two-dimensional EMD is used to separate the large and the small scales from both, the WSS fluctuations and the velocity fluctuation field. This algorithm produces physically meaningful modal representations from two-dimensional data like amplitude- or frequency-modulated signals by splitting the signal into a set of IMF based on the local characteristic time or space scales. The fluctuations of each snapshot are decomposed into a finite number of IMF until a stopping criterion is reached. The sum of these IMF represents the small scales and the remaining residual represents the large scales. The method was originally proposed by Huang et al. (1998) and details of the procedure in relation to scale separation can be found, e.g., in Agostini and Leschziner (2014).
For the investigation of the footprint of the outer LSM imposed onto the near-wall small scales, a cross-correlation between the large-scale streamwise velocity fluctuations in the outer layer $u'_{O,LS}$ and the large-scale streamwise WSS fluctuations $\tau'_{x,LS}$ is applied. Therefore, the instantaneous, large-scale velocity fluctuation field is divided into segments with the same physical size as the MPS^3 and each segment is incrementally correlated with the large-scale WSS distribution at the same time step. The value of the maximum correlation determines the superposition coefficient α (Marusic and Heuer (2007)). Its position is used to calculate the spatial delay Δx_m in the streamwise direction. With this value and the wall-normal distance z_{PIV} of the PIV measurement plane, i.e., the considered plane in the outer layer y_O, the inclination angle

$$\Theta = \arctan\left(\frac{z_{PIV}}{\Delta x_m}\right) \tag{1}$$

of the footprinting can be obtained.

4 Results

As mentioned above, it is inevitable to investigate any possible influence of the seeding particles of the PIV measurements on the behavior of the MPS^3 since both methods are applied simultaneously. Große et al. (2006) showed that the flow passing the micro pillars is well in the Stokes-flow regime, i.e, it symmetrically follows the pillar contour. However, in the unlikely event of a seeding particle colliding with a micro pillar, a possible additional micro pillar deflection due to the impact of a tracer particle on the sensor must be determined and eliminated. Theoretically, the maximum added deflection arises when the particle hits the micro pillar tip and when its kinetic energy is completely converted into deformation energy. The kinetic energy of the particle $E_{kin,p} = 0.5 m_p u_{PT}^2$ is calculated with the average mass of one particle m_p and the mean velocity at the micro pillar tip u_{PT}. Measurements of the particle diameter showed an averaged value of 1 μm in the measurement section, and using the assumption of a spherical particle and the density of the seeding fluid (*Di-Ethyl-Hexyl-Sebacat* (DEHS)), the particle mass can be calculated. Since the micro pillar can be described as a clamped cylindrical beam by linear bending theory (Große et al. (2006)), the point load arising from the impinging particle is used to calculate the micro pillar deflection. With a Young's modulus of 1.26 MPa, this results in a maximum deflection of 1.88 μm, which is roughly 1.5 times the average deflection.

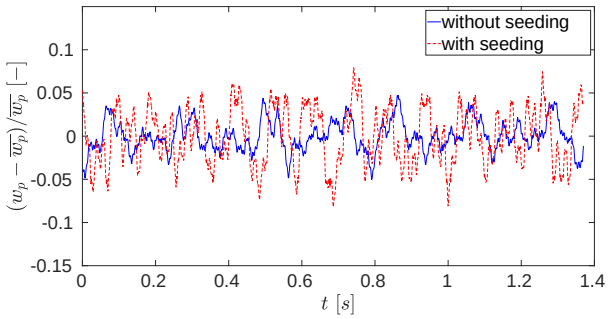

Figure 2: Time-dependent deflection of one micro pillar with and without seeding particles.

This theoretical, additional micro pillar deflection is only occasionally observed in the recorded images. Figure 2 compares the time-dependent deflection of one representative micro pillar with and without seeding particles in the flow. The mean deflection is subtracted from the instantaneous value and the result is normalized by the mean value to account for deviations of the mean WSS of both measurements. This is necessary since the number of images is not sufficient to calculate a representative average WSS due to the high temporal resolution. The fluctuations around the baseline are similar for both configurations leading to the conclusion that the typical micro pillar deflection is not influenced by the seeding particles. Nevertheless, a few exceptionally high deflections occur when seeding particles are present, e.g., at $t = 1$ s and $t = 1.258$ s, but they can easily be detected and as such eliminated. The local WSS is then calculated based on the neighboring values. The measurement without seeding also shows a few major deviations which probably arise from debris colliding with the micro pillar.
Another important influence of the seeding particles might arise from the added mass of the seeding fluid if it sticks to the micro pillar after collision. However, the mass of one seeding particle is five orders of magnitude smaller compared to the micro pillar mass. Thus, its influence is negligible. Also, no pollution of the MPS^3 by seeding fluid was optically observed during the experiments. By storing one sample in DEHS for one week, tensile tests showed no variation of the Young's modulus compared to a reference sample. Furthermore, no illumination of near-wall seeding particles by the LED system was noticed which could have effected the quality of the MPS^3 images. It is necessary to make sure that the PIV measurement plane is not oriented too close to the MPS^3 since the heat generation of the laser light sheet leads to an increased Young's modulus, which, in turn, modifies the material properties of the sensor. Succeeding MPS^3 measurements with and without seeding and laser operation did not show a noticeable influence of both components for the current location of the measurement plane.

In the following, the investigation of the near-wall small-scale dynamics and the imposed footprint by the outer LSM is presented. This analysis includes exemplary snapshot results as well as a statistical evaluation of the inclination angle.

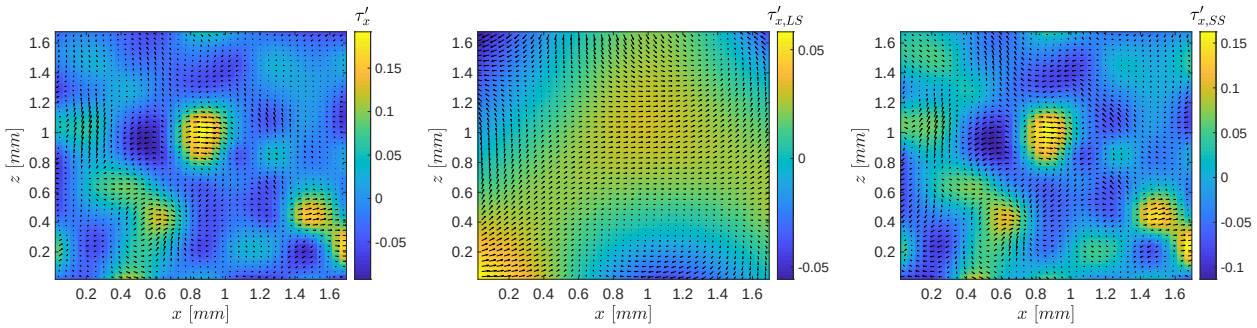

(a) WSS fluctuations τ' (b) large-scale WSS fluctuations τ'_{LS} (c) small-scale WSS fluctuations τ'_{SS}

Figure 3: Total, large-scale, and small-scale WSS fluctuations of a representative snapshot.

The mean WSS obtained by the MPS^3 measurements based on $5,484$ snapshots measures $\tau_w = 0.0992\ Pa$. This value corresponds very well to the theoretical WSS of a fully developed TCF $\tau_{w,theor} = 0.0985\ Pa$ at $Re_\tau = 925$. Figure 3 shows exemplary total (figure 3(a)), large-scale (figure 3(b)), and small-scale (figure 3(c)) WSS fluctuations for a representative snapshot. The scales are separated by a two-dimensional EMD individually performed for the streamwise and the spanwise direction. The color contours represent the corresponding fluctuations in the streamwise direction and the fluctuations in both directions are pictured by vectors. A comparison of the figures reveals that only the magnitude of the small scales is affected by the large-scale fluctuations but their character, i.e, their shape and extension, is maintained. The magnitude of the large-scale WSS fluctuations is remarkably smaller compared to the small scales.

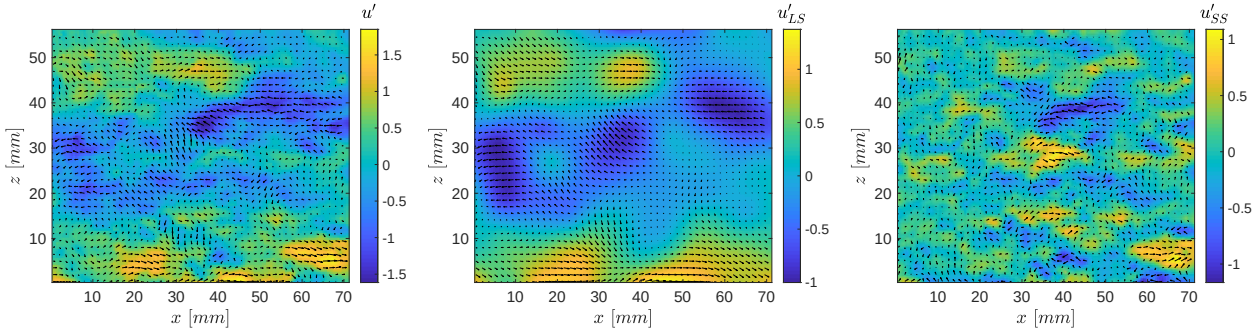

(a) velocity fluctuations u' (b) large-scale velocity fluctuations u'_{LS} (c) small-scale velocity fluctuations u'_{SS}

Figure 4: Total, large-scale, and small-scale streamwise velocity fluctuations in the outer layer of the time step shown in figure 3.

The velocity fluctuations in the outer layer obtained for the time step shown in figure 3 using the PIV measurements are displayed in figure 4. Again, the total (figure 4(a)), the large-scale (4(b)), and the small-scale fluctuations (figure 4(c)) are shown. Streamwise fluctuations are pictured by the color contours and the vectors represent the fluctuations in both directions. For clarity, only every third vector is plotted. Contrary to the WSS distribution, the magnitude of small- and large-scale fluctuations is similar and the total velocity fluctuations are not just a representation of the small-scale fluctuations magnitude-modified by the large-scale fluctuations. Figure 4(b) shows that a slow LSM meanders centrally through the field of view and is confined in the spanwise direction by two fast LSM. Since the field of view in the streamwise direction is smaller than $3h$ (Lee et al. (2014)), it is not possible to distinguish between LSM and very large-scale motions (VLSM). However, VLSM typically have a spanwise spacing of at least $1.3h$ (Abe et al. (2004),Hwang and Cossu (2010)). Since the structures captured here feature a considerably smaller spacing, they are very likely to be LSM. At the small scales, which are shown in figure 4(c), slow and fast structures are alternating in the spanwise direction with an average spacing of $\Delta z_{sp} = 15\ mm = 0.3h$ or $\Delta z^+_{sp} = 279$ in viscous scaling.

To investigate the footprint of the outer LSM imposed onto the near-wall small-scale WSS distribution, a cross-correlation between the large-scale components is performed. Figure 5 exemplarily shows the result of one time step. At first, the large-scale velocity fluctuation field (figure 5(a)) is divided into segments matching the size of the MPS^3. A square marks the position of the sensor in figure 5(a) and the WSS fluctuations of the considered time step are pictured in figure 5(c). Subsequently, each velocity segment is cross-correlated with the WSS fluctuations and the segment with the highest correlation coefficient is selected. Its position is highlighted in figure 5(a) by a square and an enlarged image is shown in figure 5(b). For the presented time step, the maximum correlation coefficient measures $\alpha = 0.9474$. It can be used to scale the near-wall influence of the large-scale streamwise velocity fluctuations at the position shifted by the inclination angle (Marusic and Heuer (2007)). The distance between the segment with the highest correlation and the position of the MPS^3 is used to calculate the inclination angle of superposition, which equals $\Theta = 10.77^\circ$ for this time step. A mean value over 500 images gives an averaged angle of $\Theta = 14.70^\circ$. Note that Agostini and Leschziner (2014) determined an inclination angle of $\Theta = 12.5^\circ$ based on DNS data of a TCF at $Re_\tau = 1,025$. Marusic and Heuer (2007) and Mathis et al. (2011) also observed inclination angles between approximately 11° to 15° in turbulent boundary layer (TBL) flows at Reynolds numbers on the order of $O\left(10^3\right) - O\left(10^6\right)$ based on HWA measurements. This leads to the conclusion that the mean angle

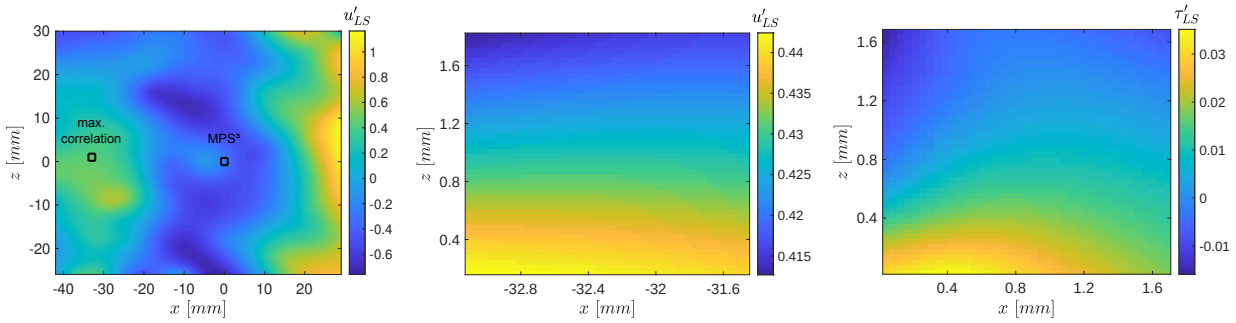

(a) velocity distribution (outer layer) (b) correlation window (outer layer) (c) correlation window (WSS)

Figure 5: (a) Instantaneous, large-scale streamwise velocity fluctuations in the outer layer, (b) segment of (a) featuring maximum correlation with large-scale WSS fluctuations, (c) instantaneous, large-scale streamwise WSS fluctuations

between the LSM and their footprint in the near-wall region is similar in TBL flows and TCF, at least for the investigated Reynolds number.

5 Conclusion

A novel approach is introduced in which the time-resolved two-dimensional WSS distribution is simultaneously acquired with the time-resolved velocity field in the outer layer of a fully developed turbulent channel flow at a friction Reynolds number of $Re_\tau = 925$. The WSS distribution is obtained with the MPS^3 and the velocity field is measured by stereo particle-image velocimetry measurements. It is observed that the seeding particles, which are needed to perform PIV measurements, only occasionally influence the micro pillar deflection. Since the impact is characterized by non-physical high micro pillar deflections, it can easily be eliminated in the post-processing.
The simultaneous measurements are used to investigate the footprints of LSM present in the outer layer of the flow on the small-scale near-wall dynamics, which, to the authors' knowledge, has never been done before experimentally in TCF. Therefore, the velocity fluctuation field as well as the WSS fluctuations are decomposed into small- and large-scale components by two-dimensional EMD. The maximum correlation coefficient of a cross-correlation between the large-scale distributions reveals the spatial delay between the LSM and their near-wall footprint. The delay is used to calculate the inclination angle, which measures $\Theta = 14.70°$ when averaged over 500 time steps. This value is similar to the angles obtained by HWA measurements in TBL flows, e.g., by Marusic and Heuer (2007) and Mathis et al. (2011). This leads to the assumption that the inclination behaves similar in TBL flows and TCF. Nevertheless, further investigations at varying Reynolds numbers have to be performed in TCF to validate this assumption.
The data will be used in the future to further investigate the near-wall small-scale modulation by outer LSM. The types of influence that are not yet considered in the current analysis, i.e., amplitude and frequency modulation as well as distortions by sweeps and ejections, will be studied in detail. Additionally, subsequent experiments at different Reynolds numbers will be performed with an enlarged MPS^3 area to capture a greater field of view.

References

Abe H, Kawamura H, and Choi H (2004) Very large-scale structures and their effects on the wall shear-stress fluctuations in a turbulent channel flow up to Re_τ= 640. *Journal of Fluids Engineering* 126:835–843

Agostini L and Leschziner M (2014) On the influence of outer large-scale structures on near-wall turbulence in channel flow. *Physics of Fluids* 26:075107

Agostini L and Leschziner M (2016) On the validity of the quasi-steady-turbulence hypothesis in representing the effects of large scales on small scales in boundary layers. *Physics of Fluids* 28:045102

Baars W, Talluru K, Hutchins N, and Marusic I (2015) Wavelet analysis of wall turbulence to study large-scale modulation of small scales. *Experiments in Fluids* 56:188

Große S and Schröder W (2009) Wall-shear stress patterns of coherent structures in turbulent duct flow. *Journal of Fluid Mechanics* 633:147–158

Große S, Schröder W, and Brücker C (2006) Nano-Newton drag sensor based on flexible micro-pillars. *Measurement Science and Technology* 17:2689

Huang NE, Shen Z, Long SR, Wu MC, Shih HH, Zheng Q, Yen NC, Tung CC, and Liu HH (1998) The empirical mode decomposition and the Hilbert spectrum for nonlinear and non-stationary time series analysis. *Proceedings of the Royal Society of London Series A: Mathematical, Physical and Engineering Sciences* 454:903–995

Hwang Y and Cossu C (2010) Self-sustained process at large scales in turbulent channel flow. *Physical Review Letters* 105:044505

Lee J, Lee JH, Choi JI, and Sung HJ (2014) Spatial organization of large-and very-large-scale motions in a turbulent channel flow. *Journal of Fluid Mechanics* 749:818–840

Liu Y, Klaas M, and Schröder W (2019) Measurements of the wall-shear stress distribution in turbulent channel flow using the micro-pillar shear stress sensor MPS^3. *Experimental Thermal and Fluid Science* 106:171–182

Marusic I and Heuer WD (2007) Reynolds number invariance of the structure inclination angle in wall turbulence. *Physical Review Letters* 99:114504

Mathis R, Hutchins N, and Marusic I (2009) Large-scale amplitude modulation of the small-scale structures in turbulent boundary layers. *Journal of Fluid Mechanics* 628:311–337

Mathis R, Hutchins N, and Marusic I (2011) A predictive inner–outer model for streamwise turbulence statistics in wall-bounded flows. *Journal of Fluid Mechanics* 681:537–566

Schäfer L, Dierksheide U, Klaas M, and Schröder W (2011) Investigation of dissipation elements in a fully developed turbulent channel flow by tomographic particle-image velocimetry. *Physics of Fluids* 23:035106